



Contents lists available at ScienceDirect

Materials Science in Semiconductor Processing

journal homepage: www.elsevier.com/locate/mssp

Review

Fabrication and characteristics of black silicon for solar cell applications: An overview

Chih-Hung Hsu^a, Jia-Ren Wu^a, Yen-Tien Lu^b, Dennis J. Flood^c, Andrew R. Barron^{d,e,f}, Lung-Chien Chen^{a,*}^a Department of Electro-optical Engineering, National Taipei University of Technology, 1, section3, Chung-Hsiao E. Rd., Taipei 106, Taiwan^b Department of Chemical and Biomolecular Engineering, Rice University, Houston, TX 77005, USA^c Natcore Technology, Inc., 87 Maple Avenue, Red Bank, NJ 07701, USA^d Department of Chemistry, Rice University, Houston, TX 77005, USA^e Department of Materials Science and Nanoengineering, Rice University, Houston, TX 77005, USA^f College of Engineering, Swansea University, Singleton Park, Swansea SA2 8 PP, Wales, UK

ARTICLE INFO

Keywords:
 Black silicon
 Solar cell
 Reflectivity
 Refractive index
 Nano

ABSTRACT

Anti-reflective (AR) coatings are a critical component of a commercially viable solar cell because by lowering reflection from the surface of the cell they enable more light to be absorbed and hence improve the power conversion efficiency of the cell. Silicon solar cells represent > 80% of present commercial cells and the most common AR coating is PECVD silicon nitride; however, recently, black silicon (b-Si) surfaces have been proposed as an alternative. Black silicon is a surface modification of silicon in which a nanoscale surface structure is formed through etching. Due to the continuous change of the refractive index of this structure surfaces with very low reflectivities are observed (~1%). This review summarizes the recent and substantial developments of black silicon for use in solar cells and discusses the advantages and disadvantages of the different methods of fabrication.

© 2014 Elsevier Ltd. All rights reserved.

Contents

1. Introduction	2
2. Methods of fabricating black silicon (b-Si).	3
2.1. Dry etching	3
2.2. Wet chemical etching	7
3. Fabrication of solar cells	10
3.1. Metal-assisted chemical etching	10
3.2. Plasma immersion ion implantation (PIII)	12
4. Comparison of synthetic methods for b-Si and solar cell efficiency	13
5. Contact formation on black silicon solar cells	13
6. Theoretical basis for the low reflectance of black silicon	14
7. Conclusions	15
Acknowledgments	15
References	15

* Corresponding author. Tel.: +886 2 2771 2171; fax: +886 2 8773 3216.

E-mail address: ocean@ntut.edu.tw (L.-C. Chen).

1. Introduction

A key requirement for an efficient solar cell is a low surface reflectance to maximize the amount of incident photons absorbed by the semiconductor to convert the incident light into electrical energy. The use of an anti-reflection (AR) coating is used to suppress the reflection of the solar cell surface by forming destructive interference of incident light. For silicon solar cells AR coatings are generally silicon nitride (SiN_x) thin films produced by chemical vapor deposition (CVD). The resulting cells have a reflectance of about 6% as compared to 40% for a polished wafer. However, AR coatings are limited in use because it only reduces the reflection for a narrow range of light wavelength and incident angle since its functionality is based on a quarter-wavelength coating. As a potential replacement for the conventional AR coating, so-called "black silicon" (b-Si) was first reported by Jansen et al. [1].

Black silicon is a surface modification of silicon where a nanoscale surface structure is formed through etching. The resulting nanoscale structure (from porous surface to bulk silicon) provides an extremely low reflectivity of close to 0% [2–4]. Because the b-Si surface nano-structure exhibits high absorption over a wide spectral range (250–2500 nm) [4,5] it offers an ideal solution as an AR coating for solar cells [6–9], as well as applications in photodetectors [10], photodiodes [11], and gas sensors [12]. The nanoscale structure may be in the form of inverted nanoscale cones (i.e., with the tip of the cones pointing upward away from the silicon surface) or a series of nanoscale pores of

varying depths and diameters extending into the surface. Both types of nanoscale structures are distributed randomly over the silicon surface.

Although originally prepared as a side effect of reactive ion etching [1], b-Si can be prepared by laser irradiation

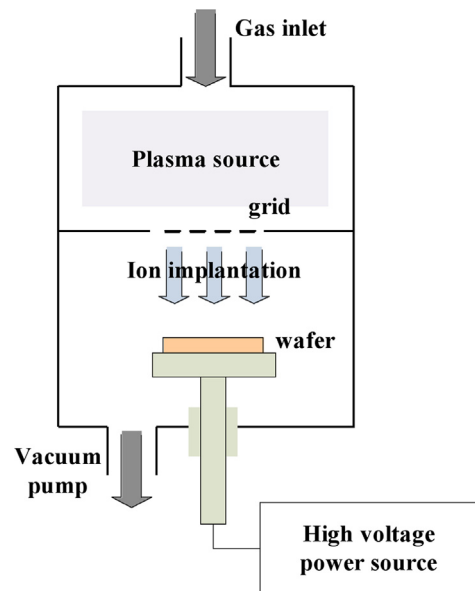


Fig. 2. Schematic illustration of a DC-plasma immersion ion implantation (DC-PIII) apparatus.

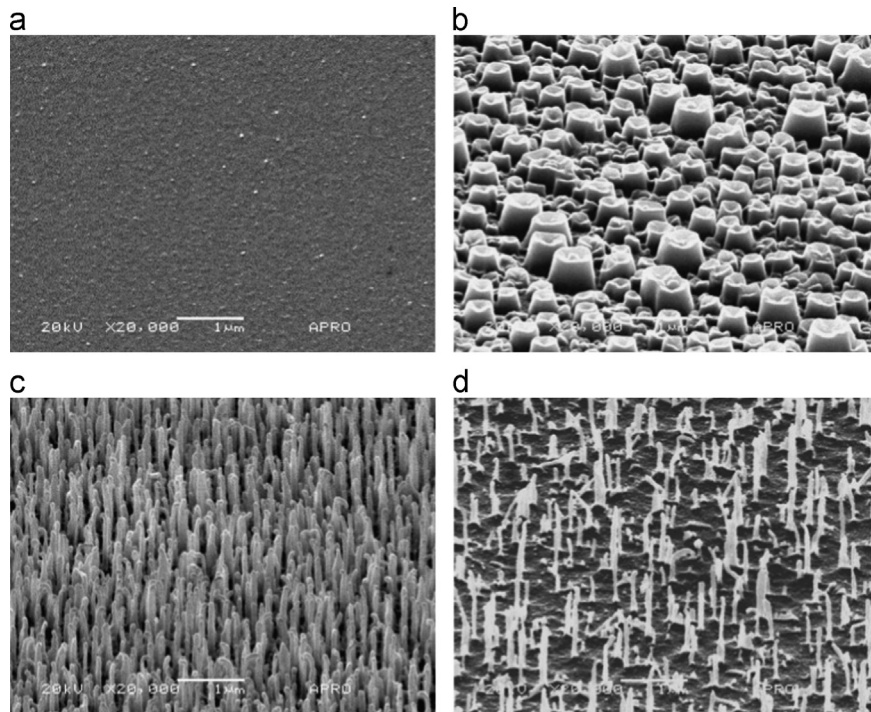


Fig. 1. SEM images of silicon surface structures formed by RIE processing with different SF_6/O_2 gas flow ratios: (a) 0.5, (b) 1.5, (c) 2.8, and (d) 4.3. RF power = 100 W and pressure = 143–302 mT. Reprinted from J. Yoo, G. Yu, J. Yi, Mater. Sci. Eng. B – Adv. 2009; 159–160: 333. Copyright (2009), with permission from Elsevier.

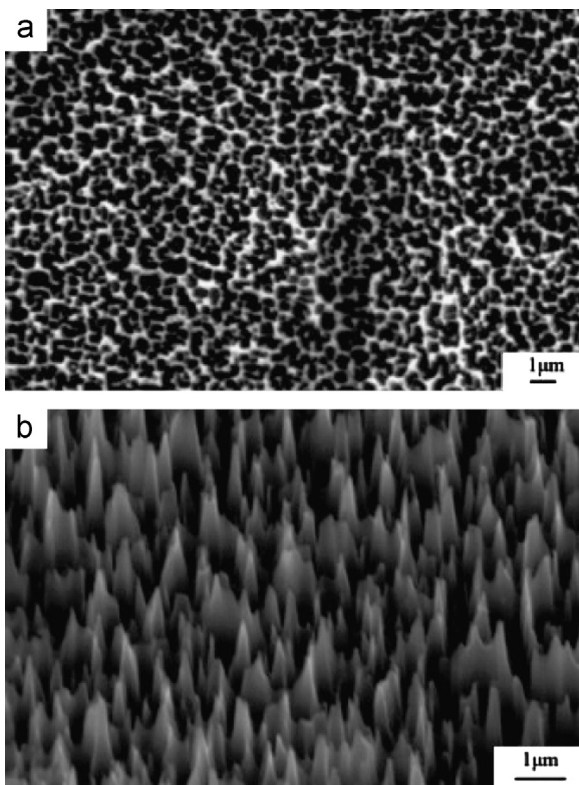


Fig. 3. SEM image of the highly uniform tapered needle-like microstructure of b-Si formed with DC-plasma immersion ion implantation (DC-PIII) using SF₆/O₂. Reprinted from Y. Xia, B. Liu, J. Liu, Z. Shen, C. Li, Sol. Energy 2011; 85: 1574. Copyright (2011), with permission from Elsevier.

[13], metal-assisted chemical etching (MACE) [14], electrochemical etching [15], and plasma dry etching [16]. The object of this review is to provide a survey of the different methods of synthesizing b-Si along with an appreciation of the merits of each method and future goals.

2. Methods of fabricating black silicon (b-Si)

The preparation methods for the fabrication of b-Si may be divided into dry and wet etching. The former involves gaseous reagents while the latter uses solution chemistry. While similar structures can be made by both methods for simplicity of discussion the two methods will be discussed using this general classification.

2.1. Dry etching

As noted above, b-Si was first prepared by reactive-ion etching (RIE) [1], and hence a significant amount of work has been done in the area. The RIE technique includes variations such as inductively coupled plasma reactive ion etching (ICP-RIE) and damage-free reactive ion etching [17]. Generally RIE uses a combination of at least two gases: the first to generate radical species that react with the silicon surface, and a second to passivate the etched surface. Sulfur hexafluoride (SF₆) is used to generate fluorine radicals (F[•]) that react with the silicon to generate volatile silicon tetrafluoride (SiF₄, Bp = -65 °C), which is removed from the surface. Sometimes SF₆ is used in-combination with chlorine (Cl₂) in which case silicon tetrachloride (SiCl₄, Bp = -67.74 °C) is formed. Oxygen radicals (O[•]) generated from oxygen react with the fresh surface to passivate the silicon

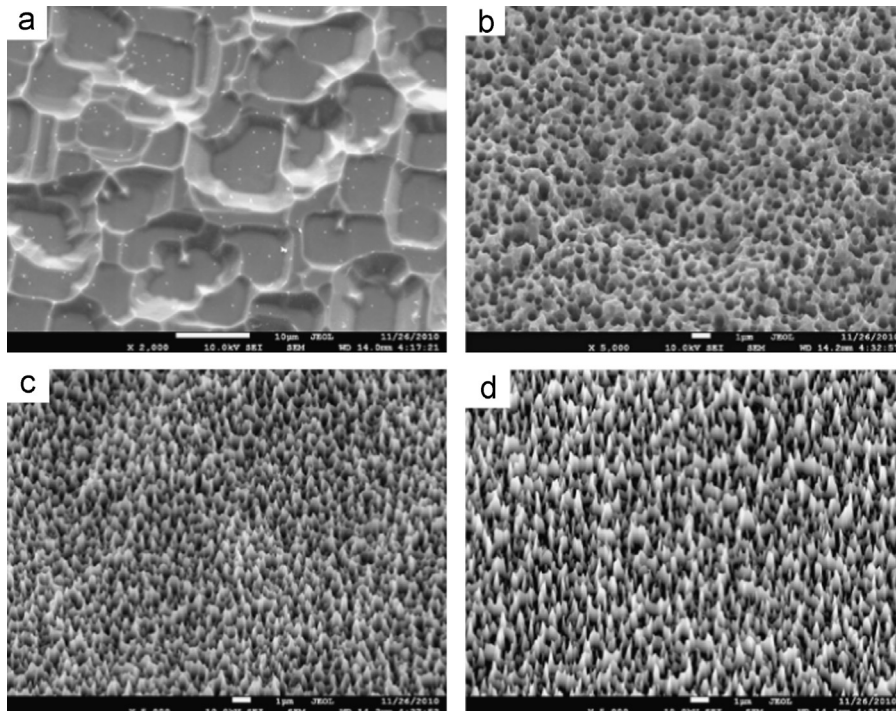


Fig. 4. SEM images of the black silicon produced by PIII process with different gas flow ratios: (a) SF₆, (b) SF₆/O₂ = 3.5, (c) SF₆/O₂ = 4.0, and (d) SF₆/O₂ = 4.5. Reprinted from Xia Y, Liu B, Zhong S, Li C, J. Electron. Spectrosc. Relat. Phenom. 2012; 184: 589. Copyright (2012), with permission from Elsevier.

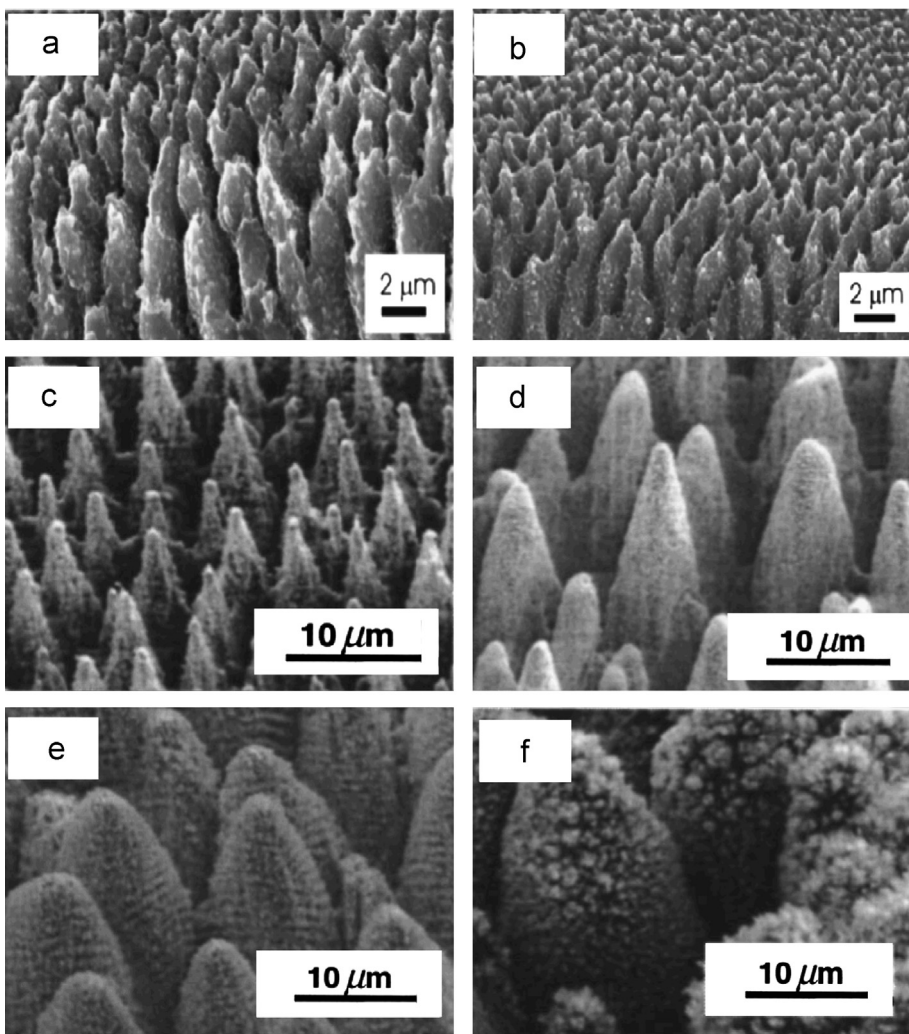


Fig. 5. SEM images of conical silicon microstructures formed in a background gas of (a) CCl_4 , (b) $\text{C}_2\text{Cl}_3\text{F}_3$, (c) SF_6 , (d) Cl_2 , (e) N_2 , and (f) air with irradiation from femtosecond laser pulses. Reprinted from C. Radu, S. Simion, M. Zamfirescu, M. Ulmeanu, M. Enculescu, M. Radou, J. Appl. Phys. 2011; 110: 034901 and R. Younkin, J.E. Carey, E. Mazur, J.A. Levinson, C.M. Friend, J. Appl. Phys. 2003; 93: 2626. Copyright (2003, 2011), with permission from AIP publishing.

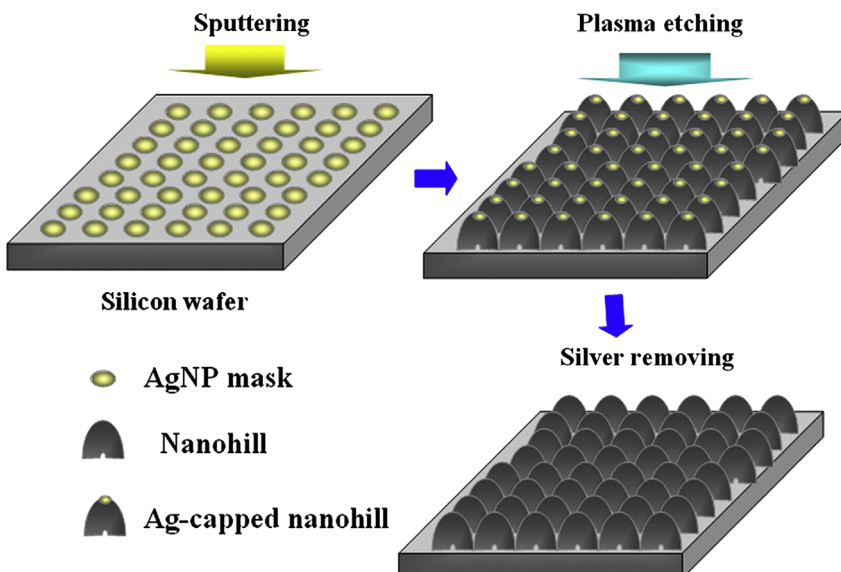


Fig. 6. Schematic of experimental procedure for plasma etching silicon surfaces using a silver nanoparticle mask. Reprinted from Y. Bi, X. Su, S. Zou, Y. Xin, Z. Dai, J. Huang, X. Wang, L. Zhang, Thin Solid Films 2012; 521: 176. Copyright (2012), with permission from Elsevier.

sidewalls to prevent further silicon etching [18–20]. Typical gas mixtures include SF₆/O₂, SF₆/Cl₂/O₂, and SF₆/O₂/CH₄. Isotropic, positively and negatively (i.e., reverse) tapered as well as fully vertical walls are achieved by controlling the plasma chemistry, RF power, and pressure [1]. For example,

Fig. 1 shows a series of SEM images of the textured silicon surfaces obtained by etching using different SF₆/O₂ gas ratios [18]. Under the conditions studied the lowest reflectance (10.29%) was obtained for the dense needle-like structure when a SF₆/O₂ gas ratio of 2.8 was used (**Fig. 1c**).

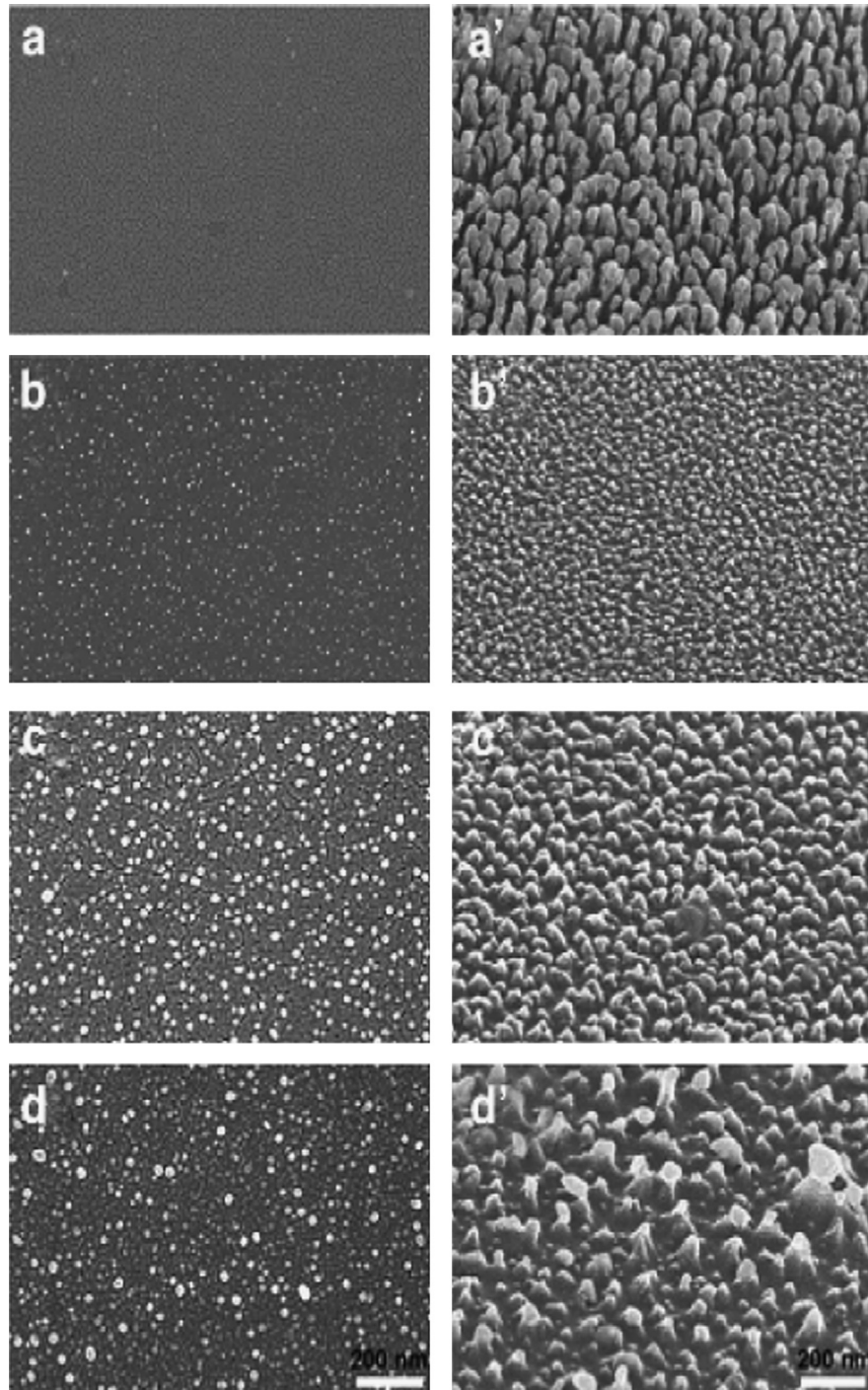


Fig. 7. Top-view SEM images of silicon substrate (left column) with different density of Ag NPs coating and corresponding as-etched silicon for 3 min (right column): (a–a') raw silicon, (b–b') 4 s, (c–c') 8 s, and (d–d') 12 s. Reprinted from Y. Bi, X. Su, S. Zou, Y. Xin, Z. Dai, J. Huang, X. Wang, L. Zhang, Thin Solid Films 2012; 521: 176. Copyright (2012), with permission from Elsevier.

A higher SF₆/O₂ gas ratio results in a sparse surface distribution of needles (Fig. 1d), while lower SF₆/O₂ ratios give large truncated cones (Fig. 1b) or with an excess of oxygen a homogeneous surface (Fig. 1a).

A further variation on RIE is the plasma immersion ion implantation (PIII) process. Like PIE, PIII uses SF₆/O₂ gas combinations, but as shown in the schematic of the PIII reactor (Fig. 2) a conducting grid is used to divide the chamber into two parts: an upper plasma region and a lower reactive region. The upper part of the chamber confines the plasma and stops the expansion of the ion sheath since the grid repels electrons that are close to it. Therefore, only positive ions diffuse into the lower part through the grid and become implanted into the wafer [21,22]. Typically, after removal of surface damage of the silicon surface with hot NaOH, the reaction gases (SF₆/O₂) react (as ions and free radicals) with the surface of the silicon substrate; a high negative voltage pulse is applied to cause the injected ions to react with the silicon substrate.

Fig. 3 shows a scanning electron microscopic (SEM) image of b-Si formed by the PIII process [23]. The surface needles that are formed are densely and uniformly distributed with a mean height of approximately 2 μm, resulting in a low reflectance (1.79%) [23]. As with the RIE process, the use of different reactive gas mixtures has a significant effect on the texture and resulting reflectance of b-Si formed by PIII. As an example, Fig. 4 shows SEM images of etched surfaces formed with a range of SF₆/O₂ ratios [24]. The use of SF₆ alone results in large etch craters (several μm across) presumably as a function of the lack of surface passivation. With the addition of oxygen to the reaction gas more nano-textured surface results. As the SF₆/O₂ gas ratio increases the morphology changes from porous (Fig. 4b) to needle-like (Fig. 4d) [24].

If laser irradiation is employed in place of plasma, then a wider range of chemical reagent may be employed to control the morphology and size of the resulting b-Si. Lasers commonly used for this purpose range from femtosecond to picosecond; however, femtosecond lasers are the most popular for preparing b-Si because the longer pulses result in significantly lower thermal ablation, owing to the melting threshold temperature of silicon [25–29]. The most commonly used laser sources are either Ti-sapphire and Nd:YLF systems [30,31], with a pulse duration of approximately 30 ~ 200 fs, with a repetition rate of 1 kHz. For research purposes, Ti-sapphire laser systems are used with wavelengths of 387, 775, 780, and 800 nm. [30,32,33]. The use of different reaction gases increases the etching rate to form different shapes and structures (e.g., Fig. 5) [5,32]. A comparison of the results using carbon tetrachloride (CCl₄) versus 1,1,2-trichloro-1,2,3-trifluoroethane (C₂Cl₃F₃) (Fig. 5a and b, respectively) and SF₆ versus Cl₂ show that the fluorine containing reaction gas produces smaller features than when chlorine is present. This variation may be due to the higher reactivity of the fluorine radical. It is interesting to note that with the use of oxygen not only are the features very large but also the surface is highly textured with oxide (Fig. 5f) [5].

In each of the dry etches discussed so far (RIE, PIII, and laser irradiation) any chemicals are used as specifically as reagents, i.e., they are present for the purpose of a

stoichiometric reaction. Also the resulting morphology of the b-Si is controlled by the reaction rates and/or relative reactivity of the reagents. In contrast, the formation of b-Si with plasma etching requires the formation of a barrier layer or etching mask. The etch mask is ordinarily formed from the surface array of silver or gold nanoparticles [16,34], although iron oxide and anode aluminum oxide (AAO) have also been used to prepare mask layers. [35,36]. A schematic of the general approach of plasma etching is shown in Fig. 6. Firstly, a layer of silver nanoparticles (Ag NPs) is deposited as the etching mask. Varying the

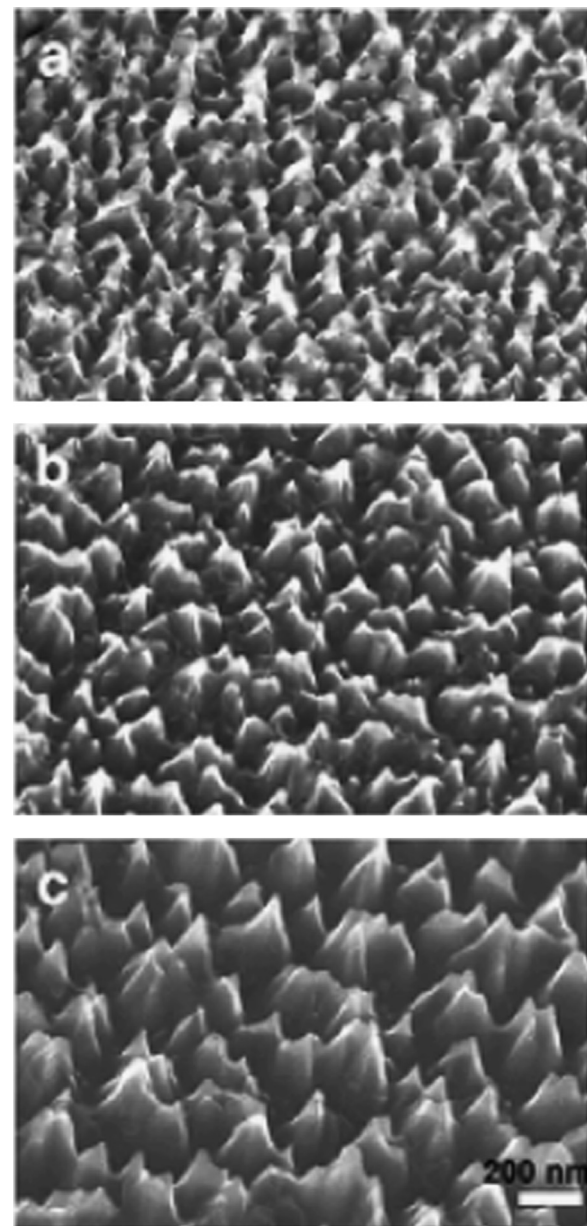


Fig. 8. SEM images of b-Si samples resulting from different etching time using the same distribution of Ag NPs as a mask: (a) 6 min, (b) 9 min, and (c) 12 min. Reprinted from Y. Bi, X. Su, S. Zou, Y. Xin, Z. Dai, J. Huang, X. Wang, L. Zhang, Thin Solid Films 2012; 521: 176. Copyright (2012), with permission from Elsevier.

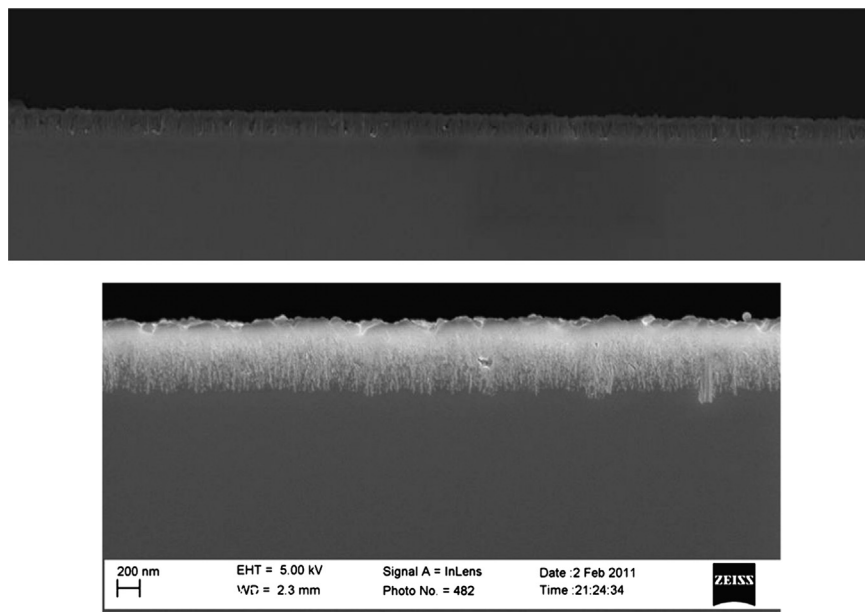


Fig. 9. Cross section of (a) Natcore-produced black silicon surface using silver nanoparticles and (b) LPD Silicon dioxide coated black silicon surface.

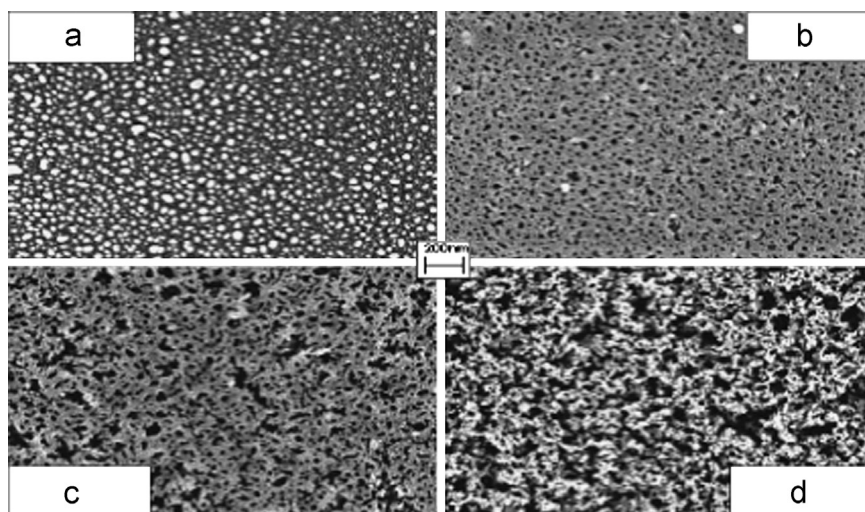


Fig. 10. SEM top-view images of the porous silicon layer produced by HF/H₂O₂/H₂O etching for (a) 0 s, (b) 3 s, (c) 10 s, and (d) 15 s. Reprinted from C. Chartier, S. Bastide, C. Lévy-Clément, *Electrochim. Acta* 2008; 53: 5509. Copyright (2012), with permission from Elsevier.

sputtering time, power source, thickness, and annealing temperature can control the size and density of Ag NPs. Next, the reaction etching gas is injected into the chamber, and a voltage is applied to the silicon substrate resulting in etching in the areas without the Ag NPs [16]. Finally, the silver is removed from the tops of the pyramids.

As may be expected the density and size of the pyramids formed by plasma etching are controlled by the distribution/concentration and size of the Ag NPs deposited on the surface of the silicon prior to etching. Fig. 7 shows a series of SEM images of silicon substrates that are coated with different densities of Ag NPs (left column) and of corresponding as-etched silicon (right column) [16]. From the relevant images it is possible to see that the

resulting b-Si surface structure is directly related to the Ag NP mask. Another critical factor in controlling the b-Si morphology during plasma etching is etching time. Under a given condition for the preparation of Ag NPs, the height of the silicon tips is proportional to etching time (Fig. 8) [16]. The height of the silicon tips increases from 106 to 222 nm as the etching time increases from 6 to 12 min, while etching for 12 min removes almost all of the Ag NPs from the surface of the silicon [16].

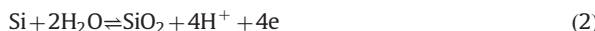
2.2. Wet chemical etching

Wet chemical etching for preparing b-Si includes both metal-assisted (metal catalyzed) chemical etching and also

electrochemical etching (see below). Metal-assisted chemical etching (MACE) generally includes electroless metallization of the surface, or deposition of pre-made metal nanoparticles, followed by etching with a solution of containing an oxidant and a complexing agent for silicon [37]. MACE overcomes the disadvantages of dry etch techniques that need either expensive instruments and high energy consumption or complicated fabricating processes, making them unfavorable for industrial applications.

The metal-assisted chemical etching method involves two steps: metal deposition and chemical etching. In the metal deposition step, a metal (such as Au, Ag, or Pt) is deposited on the Si surface as nanoparticles (NPs). The metal NPs attract electrons from the silicon surface promoting, in the presence of an appropriate oxidant, the oxidation to silica (SiO_2). In the chemical etching step, the as-formed silica is removed as H_2SiF_6 by the reaction with HF and a pit is produced under each NP. The pits become deeper and ultimately connect with each other, and the remaining Si substrate forms b-Si. Fig. 9a shows a typical cross section of a MACE-produced black silicon surface and Fig. 9b shows a MACE-produced black silicon surface that has been sealed and passivated by silicon dioxide. The SiO_2 was deposited by a wet chemical deposition technique rather than by thermal oxidation or CVD [38].

A proposed mechanism based on the working principle of galvanic cells thoroughly explains the electroless chemical etching with metal NP deposition on the Si material surface [39]. The mechanism consists of two half-cell reactions: a cathode reaction at the metal NP surface (Eq. (1)) and an anode reaction occurring at the contact point between the Si and metal NP (Eqs. (2) and (3)) [40–42]. The overall reaction is given in Eq. (4). The potential difference between the cathode sites and the anode sites results a net flux of electrons through the metal NPs and accumulation of electrons on the cathode sites. Since the cathode sites can provide more electrons for the reduction of H_2O_2 , the overall reaction (Eq. (4)) continues resulting in etching of Si under the Ag NPs. A one-step Au-assisted chemical etching method has been developed [43], in which the deposition of Au NPs and the etching of Si occurred simultaneously on the wafer surface using $\text{HAuCl}_4:\text{HF}:\text{H}_2\text{O}_2:\text{H}_2\text{O}$. The fabricated nanopore structure possessed a reflectance below 2% across a wavelength range of 300–1000 nm:



When a silicon substrate is coated with a metal thin film (such as Au, Pt, Ag or alloy) [44–48] or when it is plated by immersion in liquid (AgNO_3/HF [2,49], KAuCl_4/HF [50]), metal ions adhere to its surface and, the reactions of different metal species produce a rough surface. Different metallization procedures yield different pore sizes and pore density [51]. Different metallization conditions in AgNO_3 and KAuCl_4 solution yield different results.

The composition of the etching solution (variations of the relative amounts of HF, H_2O_2 , H_2O , or EtOH) affects the dissolution of the oxidized silicon. It is an important parameter that affects the formation and morphology of the silicon substrate. Many groups have used solutions with different compositions in metal-assisted chemical etching [52–54]. The etch time is a further variable that needs to be taken into account. For example, Fig. 10 shows various morphologies that are obtained using $\text{HF}:\text{H}_2\text{O}_2:\text{H}_2\text{O}$ with various etching times [52]. The depth of pores in the silicon substrate is linearly proportional to the etching time and the rate of penetration R_p of the Ag NPs into the bulk silicon (Eq. (5)) where Δm represents the total mass loss of the wafer; t is the etching time; S is the wafer area, and d is the wafer density [52]:

$$D = \frac{1}{2} \frac{\Delta m}{dS}; \quad R_p = \frac{D}{t} \quad (5)$$

The effects on the surface morphology and the corresponding surface reflectance caused by variation of the concentration of (1) the silver catalyst (500, 50, and 5 μM), (2) the HF and H_2O_2 concentration in the silicon etchant, (3) the $\text{HF}:\text{H}_2\text{O}_2$ ratio, and (4) etching time have been reported [55]. Lower reflectivity is a balance between sufficient silver catalyst to create large numbers of nanopores on a silicon surface and excessive silver that brings deeply etched channels that would potentially short-circuit a solar cell junction. The lowest average reflectance (0.17% over a range of 300–1000 nm) occurs with a silver ion concentration of 50 μM ; however, when the silver ion concentration decreases to 5 μM , surfaces with an acceptably low reflectance (2.60%) and a short nanopore length (< 250 nm) can be obtained with 10 min etching time. As is seen from Fig. 11, the ability to control the silver concentration, the etch solution (i.e., $\text{HF}:\text{H}_2\text{O}_2:\text{H}_2\text{O}$ ratio) and etch time allow for a wide range of reflectance values [55]. The nanopore size would increase with time as long as [HF] and [H_2O_2] are sufficient.

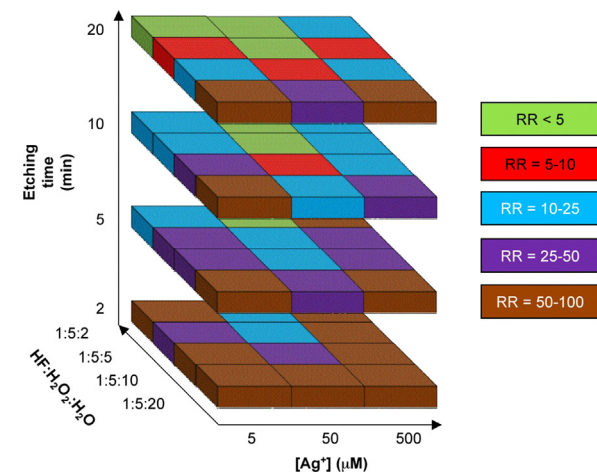


Fig. 11. Schematic plot of the average relatively reflectivity of b-Si with various $[\text{Ag}^+]$, etching time, and $\text{HF}:\text{H}_2\text{O}_2:\text{H}_2\text{O}$ ratio. Reprinted from Y.-T. Lu, A.R. Barron, Phys. Chem. Chem. Phys. 2013; 15: 9862. Copyright (2013), with permission from the Royal Society of Chemistry.

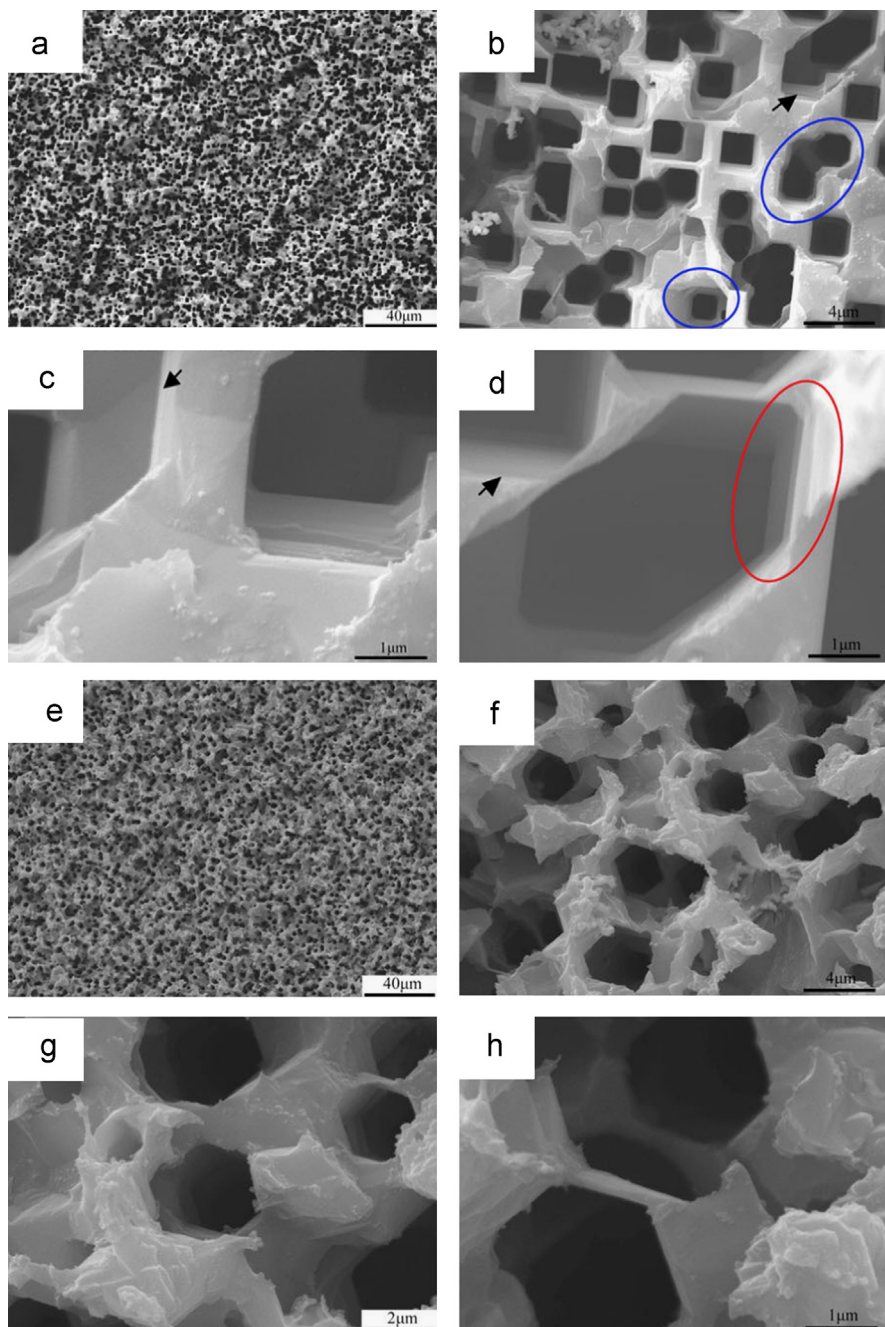


Fig. 12. SEM images of p-type silicon substrate subjected to MACE. The top macroporous layers have been removed by dipping in NaOH (1%) for 15 min. The wafers used are (100) p-type silicon substrate for (a)–(d) and (111) p-type silicon substrate for (e)–(h). Reprinted from X. Geng, M. Li, L. Zhao, P.W. Bohn, J. Electron. Mater. 2011; 40: 2480. Copyright (2011), with permission from The Minerals, Metals & Materials Society (TMS).

Geng et al. observed a pore structure when he used a solution of HF:H₂O₂:EtOH in the volume ratio 1:1:1, as displayed in Fig. 12 [56]. Quasi-ordered silicon micro/nanostructures have been obtained after 12 h of etching, and the dramatic difference between the morphologies of the (100)- and (111)-orientated silicon substrates (Fig. 12a–d and e–h, respectively) appears to reflect both the underlying crystal orientation and complex dynamical processes during etching [56].

The advantage of the electrochemical treatment over chemical etching is the control of the process is by varying the applied current density rather than alteration of the chemical speciation and reaction time. Electrochemical etching involves immersing a silicon substrate in a solvent, and applying a current for reaction. The current provides the equivalent function of the metal nanoparticle (i.e., Au or Ag) and the hydrogen peroxide (H₂O₂). Commonly used mixed solvent systems include: ethanol/H₂O/hydrofluoric acid

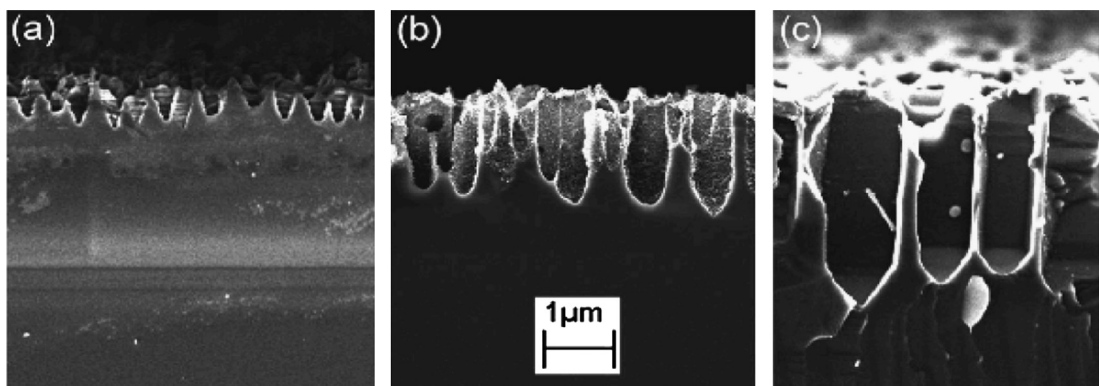


Fig. 13. Cross sectional SEM of (100) p-type silicon substrates with various resistivity after electrochemical etching: (a) $0.4 \Omega \text{ cm}$, (b) $2.5 \Omega \text{ cm}$, and (c) $12.5 \Omega \text{ cm}$. Reprinted from S. Bastide, C. Lévy-Clément, J. New Mater. Electrochem. Syst. 2006; 9: 269. Copyright (2006): with permission from J. New. Mater. Electrochem. Systems.

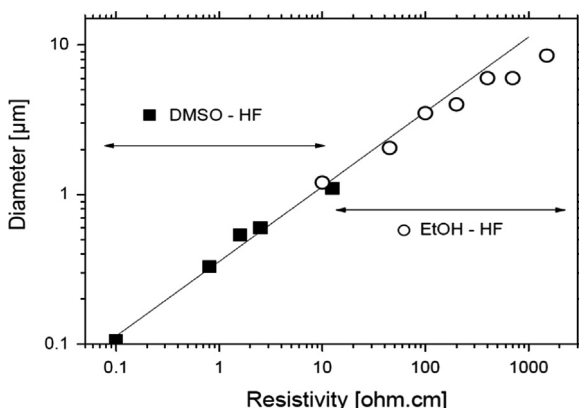


Fig. 14. Diameter of macropores formed in DMSO/HF at 5 mA/cm^2 current density (black square) and in 35% ethanol/HF at 10 mA/cm^2 current density (open circle) on (100) oriented substrates as a function of resistivity of silicon substrates. Reprinted from S. Bastide, C. Lévy-Clément, J. New Mater. Electrochem. Syst. 2006; 9: 269. Copyright (2006): with permission from J. New. Mater. Electrochem. Systems.

(HF), $\text{H}_2\text{SO}_4/\text{HF}$, HF/IPA (isopropyl alcohol)/deionized (DI) water, HF/ethanol/CTAC (cetyl trimethylammonium chloride)/DI water, and HF/DMSO (dimethyl sulfoxide) [15,57–61]. The important electrochemical etching parameters include anode current density, electrolyte solvent, and anodization time [57,60]. Several issues that are associated with the production of black silicon are as follows.

Bastide and Lévy-Clément reported that the anodization of a p-type silicon substrate in mixtures of hydrofluoric acid with specific organic solvents (in the present case either ethanol or DMSO) forms a macroporous region of the substrate, which is very efficient in reducing its reflectance [61]. Fig. 13 shows cross-sectional SEM images of (100) p-type silicon substrates with various Si substrate resistivities following electrochemical etching [61]. The nanopore diameter is directly related to the resistivity of the silicon substrate (Fig. 14) [61]. In contrast, Kim and Cho have reported that a range of vastly different morphologies

rather than just dimensionally different structures, can be prepared as a function of the silicon resistivity [58]. The surface structure of a (100) p-type silicon substrate with a resistivity ranging from 0.005 to $15 \Omega \text{ cm}$ results in ‘sponge’, ‘mountain’ and ‘column’-type morphologies (Fig. 15). Interestingly, the sponge-type structure (Fig. 15a and d) had the largest surface area per unit volume [58].

Bastide et al. studied the texturizing of silicon surfaces by electrochemical dissolution [61]. The silicon substrate was dipped in a mixture of HF with a particular organic solvent (DMSO), which caused the formation of a macroporous structure, to reduce the reflectivity. Fig. 16 shows the reflectivity spectra of a (100) grain and a (111) grain, texturized by both the electrochemical method and NaOH wet etching [61].

The use of different anodization current densities results in various vertical arrays of silicon wires and cones [59]. Fig. 17 plots the I - V curve of p-type silicon in the electrolyte solution with the morphological results at each value. In a similar manner, the anodization current density has an affect on the height and surface density of nanoparticles that are fabricated in the transition regime (Fig. 18) [60].

3. Fabrication of solar cells

3.1. Metal-assisted chemical etching

Many groups have applied the MACE process to the fabrication of silicon solar cells [3,62,63]. Srivastava et al. prepared a silicon solar cell with a silver-catalyzed nano-textured surface by the MACE process [3]. A solar cell with the nano-textured surface is formed by (i) the deposition of a thin film consisting of silver nano-islands over a silicon wafer surface by electroless metal deposition; (ii) the immersion of Ag deposited silicon wafer in $\text{H}_2\text{O}_2:\text{HF:DI}$ water in a volume ratio of 1:2:10 to form the nano-texturing surface; (iii) the diffusion of phosphorous diffusion to form an N^+ -emitter; (iv) the formation of a P^+ -back surface by aluminum-alloying, and (v) the fabrication of front and back metal contacts by evaporating a Ti/Ag bi-

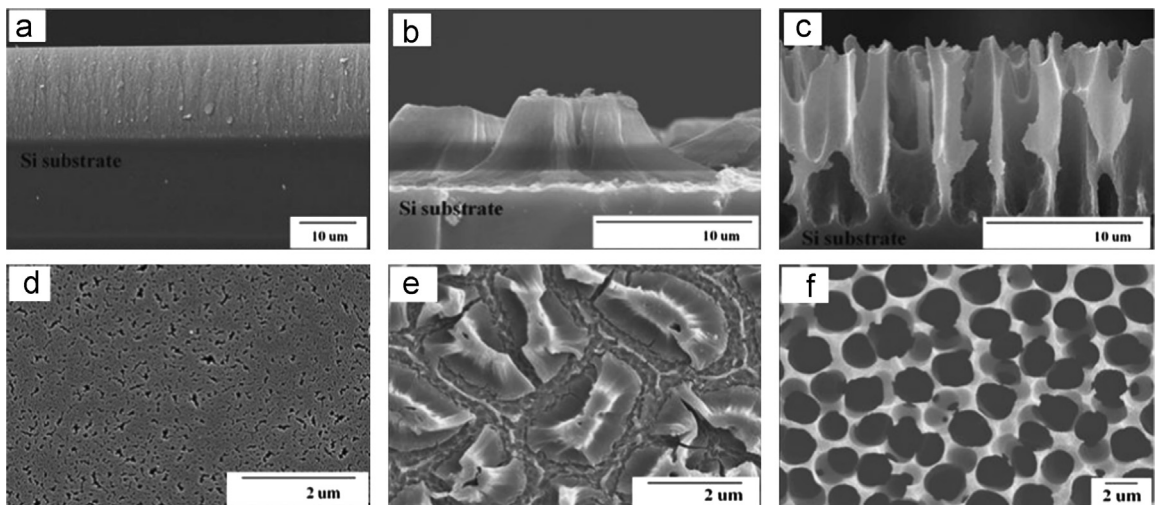


Fig. 15. Cross sectional (a–c) and plane (d–f) view SEM images of b-Si samples prepared by electrochemical etching of silicon samples with resistivity of 0.005 Ω cm (a, d), 4 Ω cm (b, e), and 15 Ω cm (c, f). Reprinted from H. Kim, N. Cho, Nanoscale Res. Lett. 2012; 7: 1. Copyright (2012): with permission from Springer.

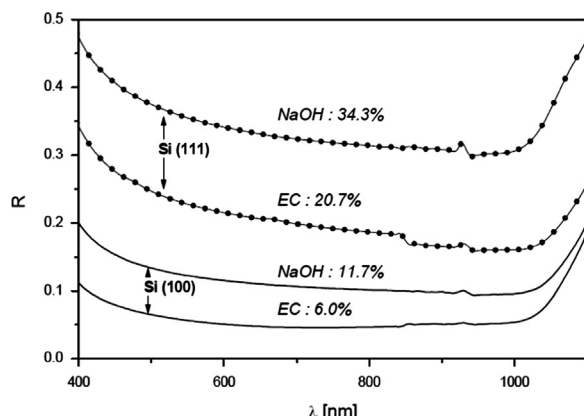


Fig. 16. Reflectance spectra of (100) and (111) silicon surface textured by electrochemical (HF/DMSO) or NaOH etching. Reprinted from S. Bastide, C. Lévy-Clément, J. New Mater. Electrochim. Syst. 2006; 9: 269. Copyright (2006): with permission from J. New Mater. Electrochim. Syst..

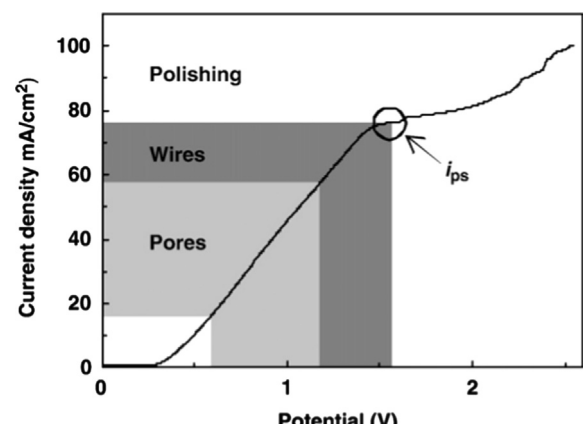


Fig. 17. A current–voltage (I – V) curve of p-type silicon in an electrolyte solution. H.S. Seo, X. Li, H.D. Um, B. Yoo, J.H. Kim, K.P. Kim, Y.W. Cho, J.H. Lee, Mater. Lett. 2009; 63: 2567. Copyright (2009): with permission from Elsevier.

layer and then sintering in a process of rapid temperature annealing. Fig. 19 schematically depicts the complete process of nano-texturing a silicon solar cell by this method. Fig. 20 shows a plot of the I – V characteristics of the illuminated control cell formed on a planar surface and on nano-textured silicon solar cells. For this particular growth methodology, the nano-textured silicon solar cell performed best in the 30 s MACE process: the short-circuit current density (J_{sc}), the open-circuit voltage (V_{oc}), the fill factor (FF), and the efficiency (E_{FF}) were 28.9 mA/cm², 0.578 V, 0.71, and 11.7%, respectively [3]. Even higher efficiencies (18.2%) have been obtained using a two-step MACE process [64].

Organic-black silicon hybrid solar cells have also fabricated. Fig. 21 displays the cross-sectional FESEM image of poly(3-hexylthiophene) (P3HT) on a nanoporous silicon substrate [65]. The P3HT film was formed on the surface of

the silicon substrate with nanostructures holes by spin coating. However, P3HT clusters with a diameter of approximately 300 nm could not penetrate into the pores in the silicon substrate to form heterojunctions, because the nanopore diameters of NPSS produced by metal-assisted nanolithography was only around 100 nm. Hence the effective contact area between the P3HT and the NPSS was much smaller than the active area of the device. Increasing the soaking time promoted the formation of the heterojunction but the viscosity of the organic solution determined the maximal efficiency. The P3HT/NPSS structure had a short-circuit current density (J_{sc}), open-circuit voltage (V_{oc}), maximum output power (P_m), fill factor (FF), and efficiency (E_{FF}), of 5.52 mA/cm², 0.345 V, 0.42 mW/cm², 0.222, and 2.82%, respectively, under a 100 W xenon lamp. However, all such samples had a high series resistance and low fill factor [65].

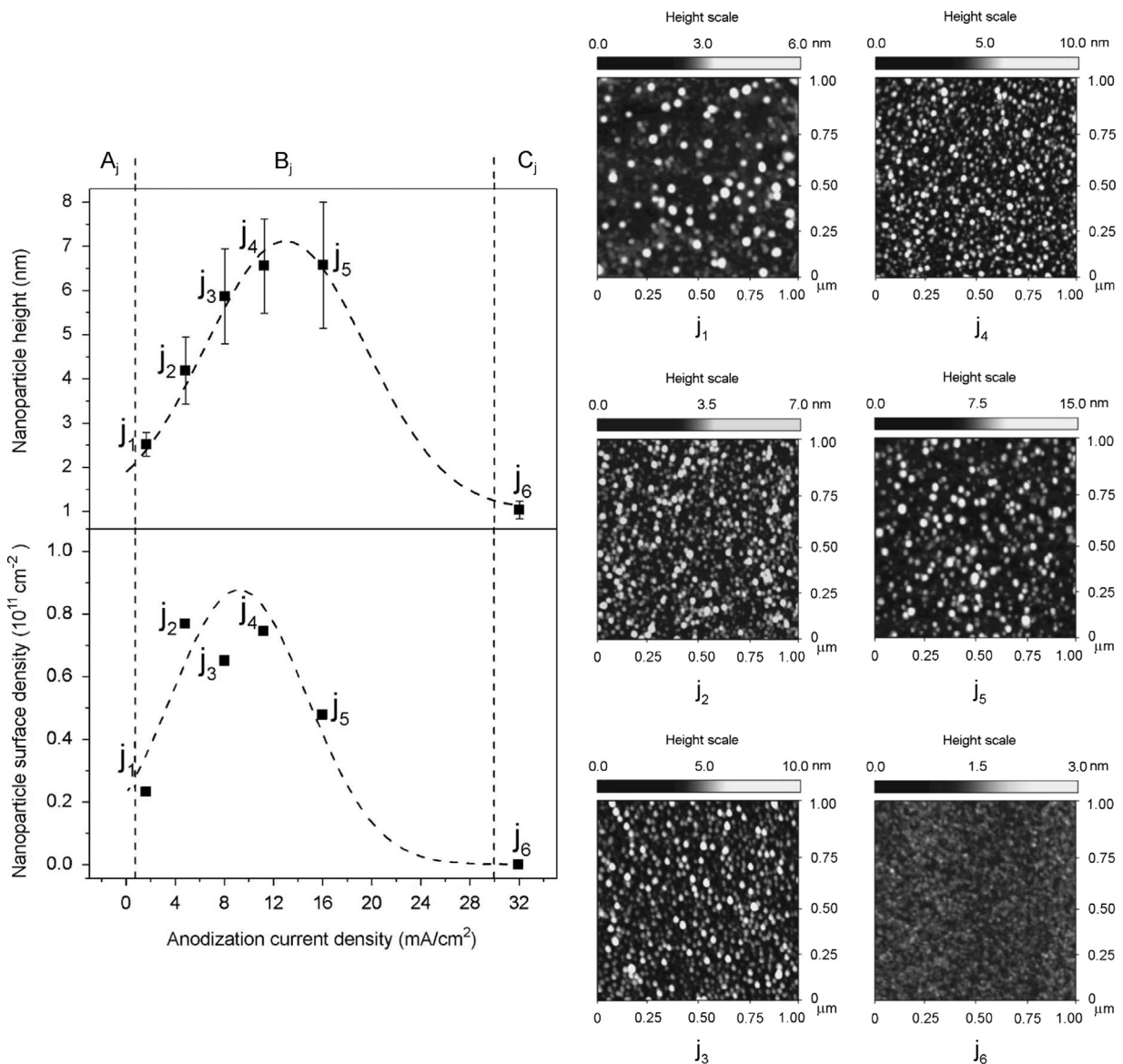


Fig. 18. Height and surface density of Si nanoparticles versus anodization current density. Regions A_j , B_j , and C_j correspond to porosification, transition, and electropolishing regimes, respectively. The same anodization time of 10 s was used in obtaining all of the results. The atomic force microscopic (AFM) images correspond to the various experimental runs are shown on the right. Reprinted from T. Nychyporuk, V. Lysenko, B. Gautier, D. Barbier, J. Appl. Phys. 2006; 100: 104307. Copyright (2006): with permission from AIP Publishing.

3.2. Plasma immersion ion implantation (PIII)

Black silicon-based solar cells have been fabricated by plasma immersion ion implantation (PIII) processes under various conditions [23,66]. Photograph of a black silicon-based solar cell with a reflectance of 1.79% by the PIII method is shown in Fig. 22 [23]. The black silicon-based solar cell had an efficiency of 15.68% with a fill factor of 0.783. In contrast, the reference cell had an efficiency of 17.5% with a fill factor of 0.78.

Solar cells with a SiN_x coating over b-Si have been reported to have a conversion efficiency of 15.99%.

Polished silicon wafers were etched to form b-Si with various texturing conditions of gas flow rate, voltage pulses, and etching time, as presented in Fig. 23. The best photoelectric conversion efficiency of the textured solar cell with a reflectivity of 3.87% was reported to be 15.99%, and that of an acid-textured solar cell was 16.59%, as presented in Fig. 24. Even though these values are similar, the series resistance of the former was higher than that of the latter because the Ag–N–Si complex layer remained on the black silicon surface [66]. The remaining Ag–N–Si complex layer between Si and Ag crystallites caused current transmission with high contact resistance. The

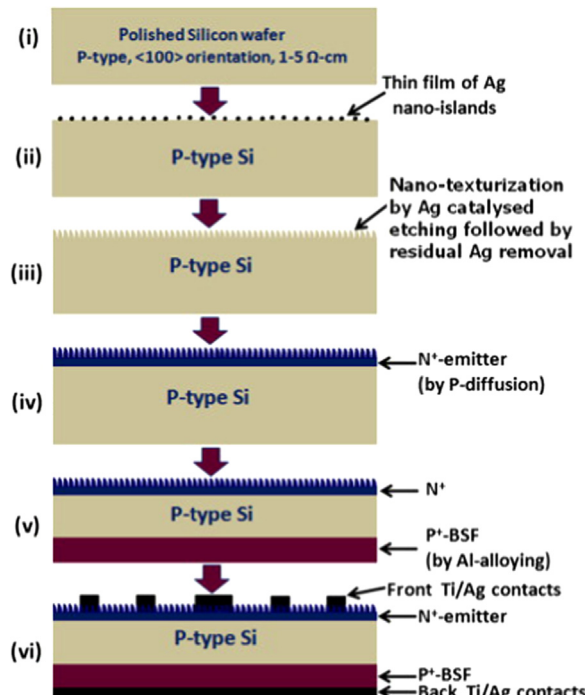


Fig. 19. Schematic of nano-textured silicon solar cells processing steps. Reprinted from .K. Srivastava, D.K. Vandana, M. Sharma, R. Kumar, P.K. Singh, Sol Energy Mater Sol Cells 2012; 100: 33. Copyright (2012): with permission from Elsevier.

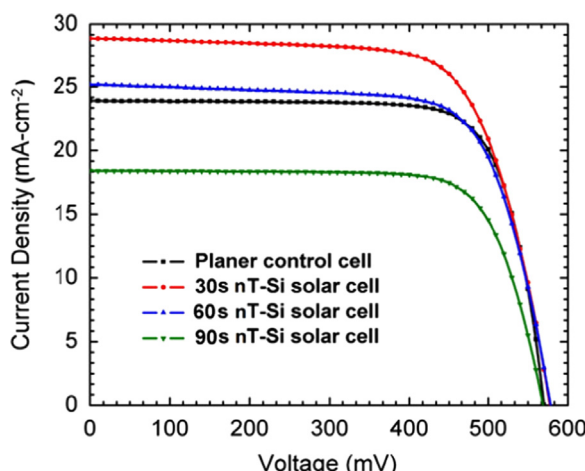


Fig. 20. Illuminated I-V curves for the planar control cell and the nano-textured silicon solar cells. Reprinted from S.K. Srivastava, D.K. Vandana, M. Sharma, R. Kumar, P.K. Singh, Sol. Energy Mater. Sol. Cells 2012; 100: 33. Copyright (2012): with permission from Elsevier.

series resistance was much worse than that of the acid-textured solar cell, owing to worse Ag-Si contact in the bottom of the nanohillocks. The conversion efficiency of the black silicon solar cell can be further improved by removing the Ag-N-Si complex layer.

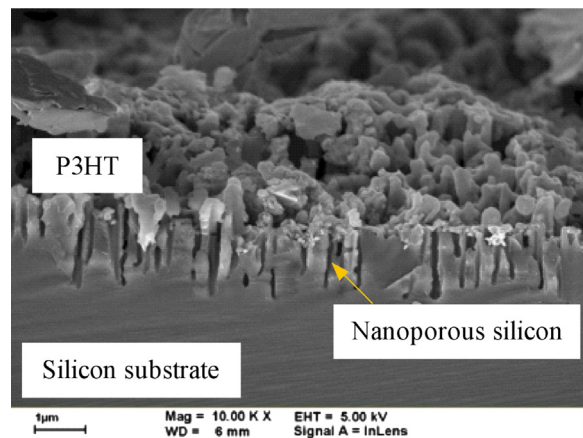


Fig. 21. FESEM cross-sectional view image of the P3HT/b-Si structure. Reprinted from L.C. Chen, C.C. Wang, J. Electrochem. Soc. 2010; 157: 405. Copyright (2010): with permission from the Electrochemical Society.

4. Comparison of synthetic methods for b-Si and solar cell efficiency

Table 1 shows a comparison of the lowest reflectivity of various b-Si samples made by different methods. We note that these comparisons are made with the understanding that the reflectance for b-Si is wavelength dependant, and these values are those reported by the various authors. However, it is worth noting that the blackest, b-Si to date has been made by a modified MACE process [67].

Table 2 compares the best-obtained parameters of solar cells that were prepared by various processes. The PIII method generally had yielded good performance, and originally it was thought that this was the better approach compared to MACE cells because of an assumed leakage current generated by the residual Ag NPs in the MACE method. However, recent work has shown that MACE cells can be made with equal efficiencies with proper attention to passivation and ensuring that the b-Si does not etch through the p/n junction. Furthermore, Branz et al. have used a two-step MACE to make cells with 18.2% efficiency.

5. Contact formation on black silicon solar cells

One issue that has been overcome is making reliable, low resistivity, screen printed contacts to black silicon solar cells. Most, if not all, laboratory cells made using black silicon anti-reflection control technology have used evaporated gold metal contacts. This sort of contact is straightforward to make and demonstrates excellent adhesion and low contact resistance. It is not, however, an acceptable contact for commercial solar cell production. The challenge of making acceptable screen printed contacts has only recently been met [68] using standard, commercially available screen-printing pastes for p-on-n solar cells. Achieving acceptable contact resistance requires careful attention to curing and sintering temperatures, ambient conditions and time at each

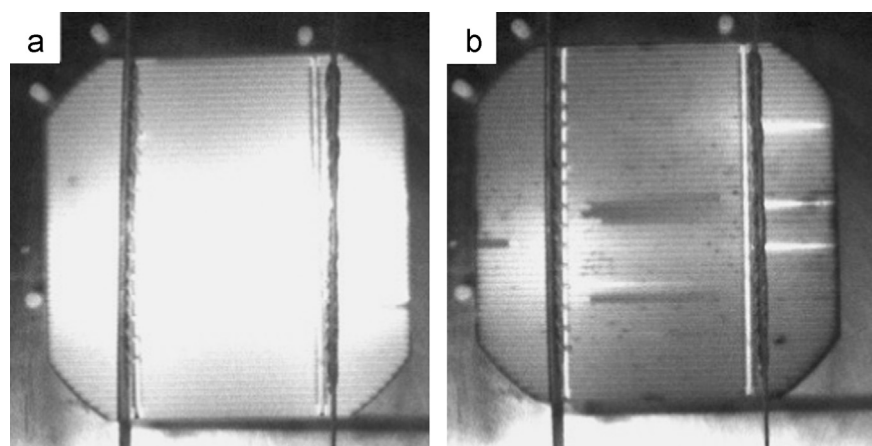


Fig. 22. The EL images of the (a) reference and (b) black silicon cell. Reprinted from Y. Xia, B. Liu, J. Liu, Z. Shen, C. Li, Sol. Energy 2011; 85: 1574. Copyright (2011): with permission from Elsevier.

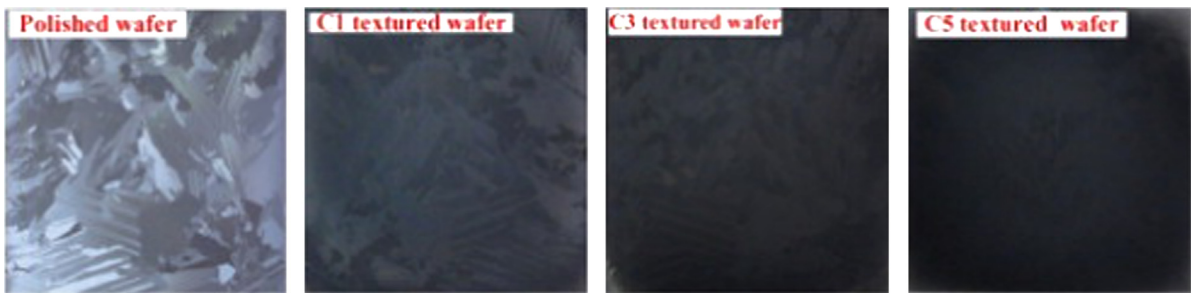


Fig. 23. Photographs of the polished silicon wafer and the black silicon wafers with the texturing conditions of C1, C3 and C5. Reprinted from S. Zhong, B. Liu, B. Y. Xia, J. Liu, J. Liu, Z. Shen, Z. Xu, C. Li, Sol. Energy Mater. Sol. Cells 2013; 108: 200. Copyright (2013): with permission from Elsevier.

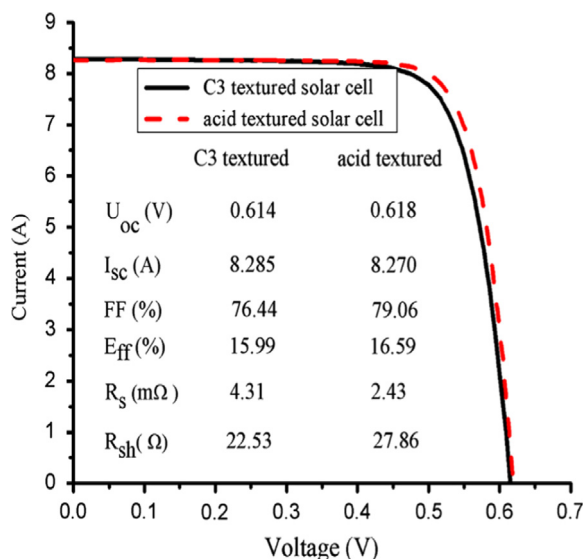


Fig. 24. Illuminated I - V characteristics of the C3 textured solar cell and acid textured solar cell. Reprinted from S. Zhong, B. Liu, Y. Xia, J. Liu, J. Liu, Z. Shen, Z. Xu, C. Li, Sol. Energy Mater. Sol. Cells 2013; 108: 200. Copyright (2013): with permission from Elsevier.

temperature. Nonetheless, a commercially acceptable process has been developed and is ready for large-scale solar cell manufacturing.

6. Theoretical basis for the low reflectance of black silicon

Contrary to what is often assumed or said, the low reflectance from a black silicon surface is not caused by light trapping. The features of such a surface whether dry etched pyramids or wet etched pores is at least an order of magnitude smaller than the wavelength of light incident on the surface. The typical situation is 10s of nm for black silicon surface features versus 100s to 1000s of nm for the wavelengths of light absorbed. An acceptable explanation can be found in the effective medium approximation (EMA) put forward by Bruggemann in 1935 [69]. Using the EMA it is possible to show that the index of refraction of a silicon surface with either type of nanoscale structure (pillars or pores) can be considered to vary essentially smoothly with depth for the black silicon surface. The elimination of any abrupt interface means that no reflection can occur, and indeed, average reflectance as low as

Table 1

Summary of different methods for the preparation of b-Si.

Synthetic method	Reagents	Mask	Catalyst	Reflectance (%)	Reference
RIE	SF ₆ /O ₂ , SF ₆ /Cl ₂ /O ₂ , SF ₆ /O ₂ /CH ₄	None	None	4	[20]
PIII	SF ₆ /O ₂	None	None	1.79	[23]
Laser irradiation	CCl ₄ , C ₂ Cl ₃ F ₃ , SF ₆ , Cl ₂ , N ₂ , air	None	None	2.5	[30]
Plasma etch	SF ₆	Ag NP	None	4.2	[16]
MACE	AgNO ₃ /HNO ₃ /HF	None	Au, Ag,	0.3	[67]
Electrochemical etching	HF, EtOH, H ₂ O	None		< 5	[15]

Table 2

Selected parameters for b-Si solar cells prepared with various methods.

Process method	V _{oc} (V)	J _{sc} (mA/cm ²)	FF	η (%)	Ref.
MACE (1 step)	0.594	32.3	76.8	14.7	[66]
MACE (2 step)	0.628	36.45	0.796	18.2	[64]
PIII	0.613	34.2	0.776	16.3	[67]

0.3% across the solar input spectrum absorbed by a silicon solar cell have been measured.

7. Conclusions

In summary, the paper has reviewed recent developments concerning black silicon and its solar cell applications. Overcoming the high series resistance effect enables highly efficient (efficiency > 18%) silicon-based solar cells with very low reflectivity (reflectivity < 1%) to be realized. The following conclusions concerning b-Si and its potential use for solar cells can be drawn. First, the low reflectivity (~1%) of b-Si makes it ideal as an anti-reflective coating. However, the nanoporous surface of black silicon substrates can cause high series resistance, and the increased surface area means that passivation of the b-Si surface is an important issue for further research. Second, b-Si single and multi-crystalline silicon solar cells have been successfully fabricated with efficiencies comparable to traditional SiN_x AR coated cells; however, making the b-Si process commercially scalable is an important goal especially as it has been determined that the adoption of MACE style b-Si processing has the potential to reduce the cost of a solar cell production by 23.5% [67]. As such b-Si represents a large step towards grid parity between solar cell technology and traditional carbon fuels.

Acknowledgments

Financial support of this paper was provided by the National Science Council of the Republic of China (Contract no. NSC 101-2221-E-027-054), the Robert A. Welch Foundation (C-0002), and Natcore Technology, Inc. (NXT.V).

References

- H. Jansen, M. de Boer, R. Legtenberg, M. Elwenspoek, *J. Micromech. Microeng.* 5 (1995) 115.
- Y. Wang, Y.P. Liu, H.L. Liang, Z.X. Mei, X.L. Du, *Phys. Chem. Chem. Phys.* 15 (2013) 2345.
- S.K. Srivastava, D. Kumar, Vandana, M. Sharma, R. Kumar, P.K. Singh, *Sol. Energy Mater. Sol. C* 100 (2012) 33.
- C.H. Crouch, J.E. Carey, M. Shen, E. Mazur, F.Y. Génin, *Appl. Phys. A – Mater.* 79 (2004) 1635.
- R. Younkin, J.E. Carey, E. Mazur, J.A. Levinson, C.M. Friend, *J. Appl. Phys.* 93 (2003) 2626.
- Y. Liu, T. Lai, H. Li, Y. Wang, Z. Mei, H. Liang, Z. Li, F. Zhang, W. Wang, A.Y. Kuznetsov, X. Du, *Small* 8 (2012) 1392.
- K. Peng, Y. Xu, Y. Wu, Y. Yan, S.-T. Lee, J. Zhu, *Small* 1 (2005) 1062.
- K. Peng, Y. Wang, S.T. Lee, *Appl. Phys. Lett.* 92 (2008) 163103.
- Z. Shen, B. Liu, Y. Xia, J. Liu, J. Liu, S. Zhong, C. Li, *Scr. Mater.* 68 (2013) 199.
- M.U. Pralle, J.E. Carey, H. Homan, S. Alie, J. Sickler, X. Li, J. Jiang, C. Palsule, J. McKee, *Proc. SPIE* 7660 (2010) 76600.
- A.M. Moloney, L. Wall, A. Mathewson, G. Healy, J.C. Jackson, *Proc. SPIE* 6119 (2006) 61190B.
- V. Mulloni, L. Pavesi, *Appl. Phys. Lett.* 76 (2000) 2523.
- C. Wu, C.H. Crouch, L. Zhao, J.E. Carey, R. Younkin, J.A. Levinson, E. Mazur, R.M. Farrell, P. Gothiskar, A. Karger, *Appl. Phys. Lett.* 78 (2001) 1850.
- X. Shen, B. Sun, F. Yan, J. Zhao, F. Zhang, S. Wang, X. Zhu, S. Lee, *ACS Nano* 4 (2010) 5869.
- L.L. Ma, Y.C. Zhou, N. Jiang, X. Lu, J. Shao, W. Lu, J. Ge, X.M. Ding, X.Y. Hou, *Appl. Phys. Lett.* 88 (2006) 171907.
- Y. Bi, X. Su, S. Zou, Y. Xin, Z. Dai, J. Huang, X. Wang, L. Zhang, *Thin Solid Films* 521 (2012) 176.
- Ü. Sökmen, A. Stranz, S. Fündling, H.-H. Wehmann, V. Bandalo, A. Bora, M. Tornow, A. Waag, E. Peiner, J. Micromech. Microeng. 19 (2009) 105005.
- J. Yoo, G. Yu, J. Yi, *Mater. Sci. Eng. B – Adv.* 159–160 (2009) 333.
- K.S. Lee, M.H. Ha, J.H. Kim, J.W. Jeong, *Sol. Energy Mater. Sol. C* 95 (2011) 66.
- D. Murias, C. Reyes-Betanzo, M. Moreno, A. Torres, A. Itzamoyotl, R. Ambrosio, M. Soriano, J. Lucas, P.R.I. Cabarrocas, *Mater. Sci. Eng. B – Adv.* 177 (2012) 1509.
- N.W. Cheung, *Mater. Chem. Phys.* 46 (1996) 132.
- P.K. Chu, *J. Vac. Sci. Technol. B* 22 (2004) 289.
- Y. Xia, B. Liu, J. Liu, Z. Shen, C. Li, *Sol. Energy* 85 (2011) 1574.
- Y. Xia, B. Liu, S. Zhong, C. Li, J. Electron Spectrosc. 184 (2012) 589.
- T.H. Her, R.J. Finlay, C. Wu, E. Mazur, *Appl. Phys. A – Mater.* 79 (2000) 383.
- X. Li, L. Chang, R. Qiu, C. Wen, Z. Li, S. Hu, *Appl. Surf. Sci.* 258 (2012) 8002.
- J. Zhu, G. Yin, M. Zhao, D. Chen, L. Zhao, *Appl. Surf. Sci.* 245 (2005) 102.
- S. Besner, J.Y. Degorce, A.V. Kabashin, M. Meunier, *Appl. Surf. Sci.* 247 (2005) 163.
- H. Liu, F. Chen, X. Wang, Q. Yang, H. Bian, J. Si, X. Hou, *Thin Solid Films* 518 (2010) 5188.
- B.K. Nayak, V.V. Iyengar, M.C. Gupta, *Prog. Photovolt. Res. Appl.* 19 (2011) 631.
- X. Bao, F. Liu, X. Zhou, *Optik* 123 (2012) 1474.
- C. Radu, S. Simion, M. Zamfirescu, M. Ulmeanu, M. Enculescu, M. Radou, *J. Appl. Phys.* 110 (2011) 034901.
- C. Wang, C.M. Lin, S. Yin, P. Ruffin, C. Brantley, E. Edwards, *Proc. SPIE* 8497 (2012). (84970W).
- T. Ghoshal, R. Sentharamaikannan, M.T. Shaw, J.D. Holmes, M.A. Morris, *Nanoscale* 4 (2012) 7743.
- L.C. Chen, B.H. Liu, *Electrochem. Solid State Lett.* 13 (2010) H108.
- S.P. Scheer, S. Ullrich, S. Kudera, C. Pacholski, *Nanoscale Res. Lett.* 7 (2012) 450.
- D. Dimova-Malinovska, M. Sendova-Vassileva, N. Tzenov, M. Kamenova, *Thin Solid Films* 297 (1997) 9.
- H.C. Yuan, J. Oh, Y. Zhang, O.A. Kuznetsov, D.J. Flood, H.M. Branz, in: *Photovoltaic Specialists Conference (IEEE PVSC)*, 2012, p. 686.
- K. Peng, A. Lu, R. Zhang, S.T. Lee, *Adv. Funct. Mater.* 18 (2008) 3026.

- [40] K. Peng, J. Hu, Y. Yan, Y. Wu, H. Fang, Y. Xu, S.T. Lee, J. Zhu, *Adv. Funct. Mater.* 16 (2006) 387.
- [41] T. Tsuboi, T. Sakka, Y.H. Ogata, *J. Appl. Phys.* 83 (1998) 4501.
- [42] X.H. Xia, C.M.A. Ashrf, P.J. French, J.J. Kelly, *Chem. Mater.* 12 (2000) 1671.
- [43] H.M. Branz, V.E. Yost, S. Ward, K.M. Jones, B. To, P. Stradins, *Appl. Phys. Lett.* 94 (2009) 231121.
- [44] A. Kurek, S.T. Barry, *Sci. Technol. Adv. Mater.* 12 (2011) 045001.
- [45] H. Fang, Y. Wu, J. Zhao, J. Zhu, *Nanotechnology* 17 (2006) 3768.
- [46] Z. Huang, N. Geyer, P. Werner, J. De Boor, U. Gösele, *Adv. Mater.* 23 (2011) 285.
- [47] M.L. Zhang, K.Q. Peng, X. Fan, J.S. Jie, R.Q. Zhang, S.T. Lee, N.B. Wong, *J. Phys. Chem. C* 112 (2008) 4444.
- [48] B. Mikhael, B. Elise, M. Xavier, S. Sebastian, M. Johann, P. Laetitia, *ACS Appl. Mater. Interfaces* 3 (2011) 3866.
- [49] X. Li, P.W. Bonn, *Appl. Phys. Lett.* 77 (2000) 2572.
- [50] K. Peng, J. Zhu, *J. Electroanal. Chem.* 558 (2003) 35.
- [51] E. Kayahan, N. Ceylan, K. Esmer, *Appl. Surf. Sci.* 255 (2008) 2808.
- [52] C. Chartier, S. Bastide, C. Lévy-Clément, *Electrochim. Acta* 53 (2008) 5509.
- [53] S. Bastide, N. Le-Quang, R. Monna, L.C. Claude, *Phys. Status Solidi C* 6 (2009) 1536.
- [54] X. Geng, Z. Qi, M. Li, B.K. Duan, L. Zhao, P.W. Bohn, *Sol. Energy Mater. Sol. C* 103 (2012) 98.
- [55] Y.-T. Lu, A.R. Barron, *Phys. Chem. Chem. Phys.* 15 (2013) 9862.
- [56] X. Geng, M. Li, L. Zhao, P.W. Bohn, *J. Electron. Mater.* 40 (2011) 2480.
- [57] D.T. Cao, LT.Q. Ngan, C.T. Anh, *Surf. Interface Anal.* 45 (2013) 762.
- [58] H. Kim, N. Cho, *Nanoscale Res. Lett.* 7 (2012) 1.
- [59] H.S. Seo, X. Li, H.D. Um, B. Yoo, J.H. Kim, K.P. Kim, Y.W. Cho, J.H. Lee, *Mater. Lett.* 63 (2009) 2567.
- [60] T. Nyhyporuk, V. Lysenko, B. Gautier, D. Barbier, *J. Appl. Phys.* 100 (2006) 104307.
- [61] S. Bastide, C. Lévy Clément, *J. New Mater. Electrochem. Syst.* 9 (2006) 269.
- [62] C.I. Yeo, J.B. Kim, Y.M. Song, Y.T. Lee, *Nanoscale Res. Lett.* 8 (2013) 159.
- [63] X. Li, Y. Xiao, J.H. Bang, D. Lausch, S. Meyer, P.T. Miclea, J.Y. Jung, S.L. Schweizer, J.H. Lee, R.B. Wehrspohn, *Adv. Mater.* 25 (2013) 3187.
- [64] J. Oh, H.-C. Yuan, H.M. Branz, *Nat. Nanotechnol.* 7 (2012) 743.
- [65] L.C. Chen, C.C. Wang, *J. Electrochem. Soc.* 157 (2010) 405.
- [66] S. Zhong, B. Liu, Y. Xia, J. Liu, J. Liu, Z. Shen, Z. Xu, C. Li, *Sol. Energy Mater. Sol. C* 108 (2013) 200.
- [67] D. Levy, personal communication.
- [68] J. Liu, B. Liu, Z. Shen, J. Liu, S. Zhong, S. Liu, C. Li, Y. Xia, *Sol. Energy* 86 (2012) 3004.
- [69] D.A.G. Bruggeman, *Ann. Phys. (Leipzig)* 24 (1935) 636.